Author Manuscript

Electro-chemo-mechanically Stable and Sodiophilic Interface for Na Metal Anode in Liquid-based and Solid-State Batteries

Enzhong Jin[1+], Jinrong Su[2+], Hongyu Hou[3+], Parham Pirayesh[1], Yijia Wang[1], Yi Yuan[1], Hanghang Yan[2], Guerman Popov[4], Lyudmila V. Goncharova[4], Sanaz Ketabi[5], Fang Dai[5], Changhong Cao[3], Lei Chen[2*], Yang Zhao[1*]*

[1]Department of Mechanical and Materials Engineering
University of Western Ontario, London, Ontario, N6A 5B9, Canada
Email: Y. Zhao: yzhao628@uwo.ca

[2]Department of Mechanical Engineering
University of Michigan−Dearborn, Dearborn, MI, 48128 USA
Email: L. Chen: leichn@umich.edu

3 Department of Mechanical Engineering
McGill University, Montreal, Quebec H3A 0C3, Canada
Email: C. Cao: changhong.cao@mcgill.ca

[4]Department of Physics and Astronomy
University of Western Ontario, London, ON N6A 3K7, Canada

[5]General Motors Research and Development Center
30470 Harley Earl Boulevard, Warren, Michigan 48092, United States

Abstract

Na metal batteries (NMBs) are attracting increasing attention because of their high energy density. However, the widespread application of NMBs has been hindered by the growth of Na dendrites and interface instability. The design of artificial solid electrolyte interphase (SEI) with tuned chemical/electrochemical/mechanical properties is the key to achieving high-performance NMBs. In this work, we developed a metal-doped nanoscale polymeric film with tunable composition, sodiophilic sites and improved stiffness. The incorporation of metal crosslinkers in the polymer chains results in exceptional electrochemical stability for Na metal anodes, leading to a significantly prolonged lifespan even at high current densities, which is at the top of the reported literature. The mechanical properties measurements and electro-chemo-mechanical phase-field model are performed to interpret the impact of the

This is the author manuscript accepted for publication and has undergone full peer review but has not been through the copyediting, typesetting, pagination and proofreading process, which may lead to differences between this version and the Version of Record. Please cite this article as doi: 10.1002/adma.202406837.

This article is protected by copyright. All rights reserved.

ionic transportation capability (decoupled mechanical) and mechanic property in the metal-doped polymer interface. In addition, our approach provides a promising strategy for the rational design of electrode interfaces, providing enhanced mechanical stability and improved sodiophilicity, which can open up opportunities for the fabrication of next-generation energy storage.

Introduction

Li-ion batteries (LIBs) are the most widely used energy storage systems for various applications, including portable devices and electric vehicles (EVs). However, lithium, the crucial element in LIBs, will face supply shortages and the prices of lithium compounds have increased dramatically in recent years [1]. Na batteries are an ideal complementary technology to LIBs because of their high abundance, low cost and suitable redox potential of Na [2]. Among different types of Na batteries, Na metal batteries (NMBs) with Na metal anode attracted increasing attention because of the high energy density (e.g., theoretical energy density ~1274 Wh kg^{-1} for room temperature Na-S batteries) compared to Na-ion batteries (100~150 Wh kg^{-1}) and even LIBs (350~400 Wh kg^{-1}) [3]. Na metal is an ideal choice among all the possible anodes with a high theoretical specific capacity (1166 mAh g^{-1}) and low electrochemical potential ($Na^+/Na = -2.7$ V vs. SHE) [4]. However, several challenges hinder their further applications, including Na dendrite and dead Na layer formation, undesirable side reactions with electrolytes, and infinite volume change [5]. One of the keys to addressing those issues is to achieve stable interfaces between the Na metal anode with the electrolytes. Naturally, the highly reactive Na metal will react with the electrolytes chemically and electrochemically to form the solid electrolyte interphase (SEI), resulting in increased resistance and serious dendrite formation [6]. Different strategies have been reported to fabricate artificial SEI to stabilize the interface of metallic Na with reduced dendrite formation and enhanced electrochemical performances [4b, 7].

The ideal artificial SEI layer for Na metal anode should possess the features including i) chemical/electrochemical stability toward electrolytes; ii) good mechanical stability to accommodate volume change; and iii) presence of sodiophilic sites for regulating the Na deposition; iv) optimized physical properties of the coating, such as being ultrathin (close to a few nanometers), uniform and continuous [8]. Many previous studies are dedicated to the influence of chemical and electrochemical stabilities on the interfaces. The chemical/electrochemical stable interfaces, such as metal oxide, metal fluoride, solid-state electrolytes (SSEs), and polymers, are expected to prevent the side reactions between the

This article is protected by copyright. All rights reserved.

Author Manuscript

reactive Na metal with electrolytes and reduce the dendrite and dead Na formation during cycling [9]. Early research has demonstrated that the fabrication of organic-inorganic composite protective layer (such as poly(vinylidene fluoride) (PVDF)-Sn and PVDF-NaF films) with high mechanical modulus can effectively suppress the Na dendrite formation and enhance the electrochemical performances [10]. However, the influences of mechanical stability on the Na dendrite formation and electrochemical performances haven't been studied in detail. Meanwhile, the design and fabrication of nanoscale protective layers for Na metal anodes with good mechanical stability are in their infancy. Strategies for artificial SEI design on Li metal anode provide essential insights for engineering artificial SEI for Na metal anode. Different mechanical properties need to be considered for establishing mechanically stable protective layers of Li metal anodes, such as elastic modulus, toughness, fracture toughness, fracture stress, etc [11]. For example, a moderate elastic modulus (e.g. SEI layer with Young's modulus of ~5.2 GPa) is essential for suppressing the dendrite growth and preventing plastic deformation on the interface [12]. The toughness of the interfaces is an important indicator of the capability of the layer for accommodating the volume change during cycling. Constructing organic-inorganic hybrid films is a promising approach to realizing mechanically stable interfaces for Li metal anode [13]. Organic coatings are considered to be more effective than inorganic coatings due to their greater flexibility, but usually, organic coatings have low stiffness [14]. The hybrid films inherit the advantages of both inorganic and organic layers, presenting promising properties to be used as interfaces for Li metal anode [15]. For example, a Cu_3N-styrene butadiene rubber hybrid film was reported as the artificial SEI for Li metal anode [16]. The inorganic phase of Cu-Li_3N imparted mechanical stiffness that prevented the propagation of Li dendrites. Meanwhile, the polymeric phase ensured the film's intactness and prevented cracking during battery cycling. In addition, two types of nanoscale hybrid films were designed and demonstrated with dual-layer and nanoalloy structures for Li metal anode, respectively [17]. It was found that the hybrid interfaces with higher stiffnesses and failure forces led to reduced Li dendrite formation and prolonged electrochemical performances. The importance of interfacial mechanical properties is gradually recognized and emphasized for the study of metal anodes.

Sodiophilic sites are widely used in 3D hosts for regulating Na deposition and reducing dendrite formation. Generally, two types of sodiophilic sites were reported in the nanostructure hosts. The first type is to create dopants on nanocarbon structures, such as N, S, O, etc. For example, the pyridinic and pyrrolic sites with three N atoms provide stronger

This article is protected by copyright. All rights reserved.

Author Manuscript

binding energy with Na, resulting in the better adsorption of Na ions. The Na ions will plate as metallic Na atoms on the sodiophilic sites of the dopants [18]. Another approach is to introduce the sodiophilic metal or metal oxide particles, such as Au, Ag, Zn, Sn etc., in the 3D hosts to stabilize the Na plating/stripping [19]. Among the candidates, Au and Ag are the two most popular metals as sodiophilic sites with low nucleation potential [20]. However, the costs of Au and Ag are very high, which hinders practical applications. Furthermore, Li-based SnS graphene nanocomposite membrane as an artificial SEI layer allows cyclability of Na metal by suppressing dendrite formation and enhancing stability [21]. Zn metal can form the $NaZn_{13}$ alloy, which is sodiophilic for Na metal deposition and more economically friendly.

Herein, we design and fabricate a new hybrid protective layer for the Na metal anode, aiming to meet all the requirements of an ideal artificial SEI. A metal-doped hybrid polyurea (PU) film with tunable composition, sodiophilic sites and improved stiffness was fabricated by introducing Zn or Al as crosslinkers into the polymer chains and adopted as an artificial SEI for Na metal. Compared to bare Na and pure PU-coated Na, the Na metal anode coated with the metal-doped PU film exhibits significantly improved electrochemical performance. Specifically, Zn-doped PU of optimized thickness effectively prevents the formation of dendritic structures and enables uniform Na plating and stripping. This leads to a prolonged lifetime of the Na metal anode, even under ultra-high current density conditions of 10 mA cm^{-2} in symmetrical cells. In addition, the inclusion of Zn ions in the film promotes a uniform flux of Na ions on the surface of the Na metal, while also facilitating the formation of a stable SEI. The electrodeposition model with elaborate structure demonstrates that metal-doped film with great ionic transportation capability can enable more homogeneous deposition due to faster ion diffusion. The electro-chemo-mechanical phase-field model proves that the film with excellent mechanical stability can generate sufficiently high compressive stress to inhibit dendrite growth. Overall, our findings demonstrate the potential of utilizing ultra-thin metal-doped polymer films as protective layers to achieve stable and long-lasting Na metal anodes. By introducing this concept, we open new avenues for the development of advanced protective coatings for Na metal anode energy storage systems, offering improved performance and enhanced stability.

Results and Discussion

This article is protected by copyright. All rights reserved.

Author Manuscript

Author Manuscript

The pure polyurea (PU) films using ethylenediamine (ED) and 1,4-phenylene diisocyanate (PDIC) as precursors have been deposited by MLD techniques before. [22] To fabricate the robust protective layer, we designed experiments to study two different single metal dopants (Al or Zn) effects for artificial SEI. By introducing trimethylaluminum (TMA) as Al-crosslinkers and diethylzinc (DEZ) as Zn-crosslinkers into the PU, the dative bonds of Al-N and Zn-N are formed by the reactions (TMA-ED) and (DEZ-ED), following by the urea bonds from the reaction between PDIC and ED, as shown in Figure 1(a) [14]. For the metal-doped PU film, we fabricated this layer with different deposition cycle numbers including 10, 25 and 50 cycles. The samples are named Na@nAl, PU and Na@nZn, PU (n = MLD cycle number), respectively. For example, the sample with 50 cycles of MLD Zn-doped PU layer is named Na@50Zn,PU and the sample with 25 cycles of MLD Al-doped PU layer is named as Na@25Al,PU. The MLD pure PU named as Na@nPU is used for reference samples as the baseline for comparison. The deposition temperature of MLD metal doped PU on the Na metal anode was controlled at a relatively low temperature (65 °C).

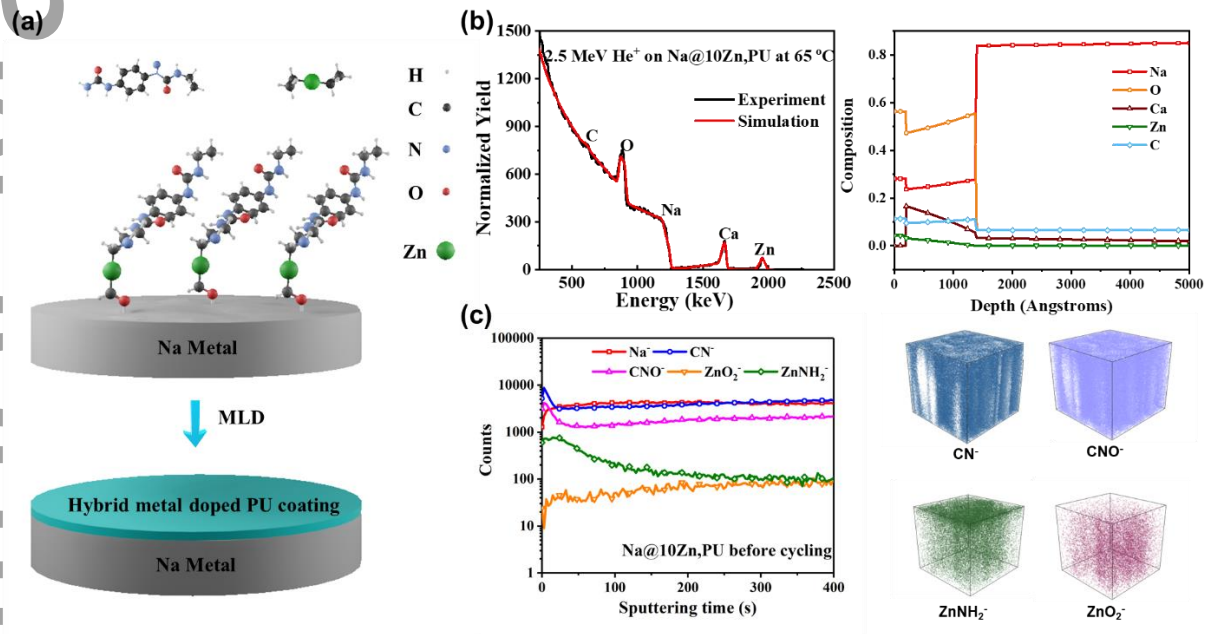


Figure 1 a) Schematic diagram showing the MLD process to fabricate metal dopant hybrid polyurea coating on Na metal anode. b) The RBS spectra and simulated depth profiles of Na@10Zn,PU. c) The ToF-SIMS secondary ion images, the depth profile of various secondary ion species and corresponding 3D rendering images of Na@10Zn,PU.

Rutherford backscattering spectrometry (RBS) and time-of-flight secondary ion mass spectrometry (ToF-SIMS) are used, as shown in Figures 1(b), (c), and Figures S1-S4, to study

This article is protected by copyright. All rights reserved.

the thicknesses and chemical compositions of the artificial SEI layers. Figure 1(b) presents the RBS spectra and simulated depth profile of Na@10Zn,PU. The RBS C, Zn surface peaks confirm the successful synthesis of the Zn-containing hybrid coating layer on Na metal. Based on the elemental depth profile model for the best RBS spectra fits, the thickness of the top layer of Na@10Zn,PU is about 19 nm (~1.9 nm/cycle). The intensity of the Al peak of Na@25Al,PU is lower than the Zn peak as shown in Figure S1, as the intensity of the RBS peak is proportional to the atomic number of the element squared (~Z^2). The thickness of the top layer of Na@25Al,PU is about 20 nm, whose average thickness per cycle is 0.8 nm/cycle. The different growth rates between two metal-doped PU layers are due to the difference in atomic radius between Zn and Al. The N peak observed indicates the presence of PU film deposited on the surface of Na metal, as shown in Figure S2. The thickness of a top layer of Na@50Pu is about 50 nm observed from the simulated depth profile. Moreover, the Ca surface peak can be detected in the RBS spectra, which could be considered as an impurity from chemical sources.

ToF-SIMS measurement results of Na@10Zn,PU, Na@25Al,PU, Na@50PU are shown in Figure 1c, Figure S3 and Figure S4, respectively. Figure 1c presents the top surface secondary ion images, depth profiles, and corresponding 3D rendering reconstructed images of CN^-, CNO^-, ZnO_2^-, $ZnNH_2^-$ for Na@10Zn,PU. $ZnNH_2^-$ ions are generated from Zn-crosslinkers in the hybrid polyurea and CNO^- and CN^- are derived from the urea bond of the polyurea matrix. With an extended sputtering time, the concentration of all three ions (CN^-, NCO^-, and $ZnNH_2^-$) decreases and eventually reaches a plateau. In parallel, the signal of Na^- experiences an initial decrease followed by a subsequent increase, indicating the gradual appearance of bulk Na as the coating layers are progressively removed through sputtering. In addition, the thickness of Na@10Zn could also be obtained from the ToF-SIMS depth profile where the signal of $ZnNH_2^-$ decreases after around 100 s sputtering time (Cs^+ sputtering rate 0.2 nm s^{-1}) corresponding to around 20 nm top layer thickness which is consistent with the simulation results from RBS [23]. Na@25Al,PU and Na@50PU shown in Figure S3 and Figure S4 present similar trends with the results of Na@10Zn,PU. The signal of AlO_2^- of Na@25Al,PU increases and remains constant after around 100 s, corresponding to the top layer thickness from RBS results as well. In the depth profile of Na@50PU, as expected, the signals of CN^- and CNO^- decrease to a plateau after 200 s, while the signal of Na^- shows the opposite trend starting to increase and remaining constant after 250 s of Cs^+ sputtering, demonstrating that the chemical composition and the thickness of pure PU film agree well

This article is protected by copyright. All rights reserved.

Author Manuscript

with the RBS results. Nevertheless, it is important to note that the secondary ion signals obtained from ToF-SIMS represent only an approximate estimation due to the surface roughness of Na metal foils.

To understand the surface chemistry and composition of metal-doped PU coating, we have conducted X-ray photoelectron spectroscopy (XPS) on Na@10Zn,PU Na@25Al,PU and Na@50PU (Figure S5, S6 and S7). Figure S5(a) shows the Zn $2p_{3/2}$ spectrum demonstrating a notable portion of Zn in the polymer film is +2 oxidation state, with a fraction also found in the 0-oxidation state, indicating the formation of the alloy with Na metal [24]. In Figure S5(b), the C 1s spectrum reveals distinctive peaks corresponding to C=C (at 283 eV), C–C/C–H (at 248.8 eV), C=O (at 288 eV), and C-N (at 286.3 eV) bonds originating from the polymer chain backbone which are consistent with reported literature.[25] Two distinct types of N chemical bonds are evident in the N 1s spectrum shown in Figure S5(c): N–C=O bonding (at 400 eV), attributed to urea groups, and minor N=C bonding (at 398 eV), originating from the isocyanate terminal groups.[25-26] Figure S5(d) shows the O 1s spectrum consisting of N-C=O (at 531 eV) and C-O chemical bonds (at 534 eV) from polyurea.[25b] In addition, Na KLL Auger peak (at ~536.0 eV) can be observed in the O 1s spectrum which originates from the chemical interaction between the coating film and Na metal anode.[27] The XPS spectra of C 1s, N 1s, and O 1s for Na@25Al,PU (Figure S6)and Na@50PU (Figure S7) exhibit nearly identical binding energies for each chemical bond as observed in Na@10Zn,PU including C–N, C=O, N-C=O bonds from polyurea matrix.[24, 25b] XPS spectrum results confirm the chemical composition of the PU matrix and metal crosslinkers Na@10Zn,PU and Na@25Al,PU, as well as the interaction between film layers and the Na metal surface.

Author Manuscript

This article is protected by copyright. All rights reserved.

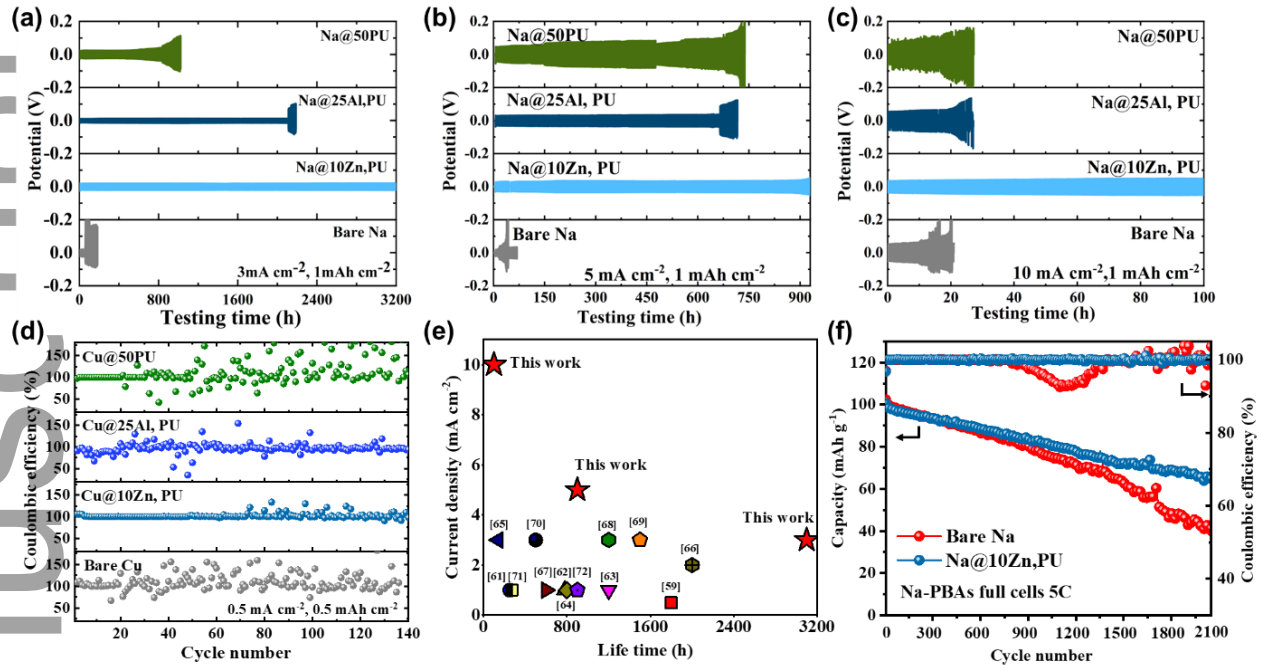


Figure 2 The overpotential of Na/Na symmetric cells using bare Na foil and Na@10Zn,PU, Na@25Al,PU, and Na@50PU in the ether-based electrolyte at the current density of a) 3 mA cm^{-2}, b) 5 mA cm^{-2}, and c) 10 mA cm^{-2} with the capacity of 1 mAh cm^{-2}. d) Evaluation of Coulombic efficiency (CE) of bare Cu, Cu10Zn,PU, Cu@25Al,PU, and Cu@50PU in Cu-Na cells at current densities of 0.5 mA cm^{-2} with a capacity of 0.5 mAh cm^{-2}. e) Comparison of the life time with different current densities but the same capacity (1 mAh cm^{-2}) obtained in this work with the values reported in recent studies. (f) Cycling performance of Na-PBAs full cells at a rate of 10C (1 C represents 170 mA g^{-1}) using bare Na and Na@10Zn,PU.

Symmetrical cells using ether-based electrolyte (1M $NaCF_3SO_3$ dissolved in diethylene glycol dimethyl ether (DEGDME)) were assembled to evaluate the Na plating/stripping behavior and electrochemical performance of the different thickness designs of the coating layers on Na metal anodes. Figure S8-S10 show the electrochemical performances of the Na@nZn,PU, Na@nAl,PU and Na@nPU (n=5, 10, 25, 50) with different layer thicknesses in the symmetrical cells, which determine the optimization layer thickness of each group. All of these cells were cycled under the current density of 3 mA cm^{-2} with the capacity limitation of 1 mAh cm^{-2}. In the group of Zn-doped PU layer-coated Na metal foils, the Na@10Zn,PU exhibits the best performance with an overpotential of ≈ 20 mV (vs Na^+/Na) over 3000 h, as shown in Figure S8. The Al-doped PU layer samples (Na@nAl,PU) were also investigated

This article is protected by copyright. All rights reserved.

Author Manuscript

under the same conditions, and the electrochemical performances are presented in Figure S9. Among all samples of different thicknesses, the Na@25Al,PU presents the longest lifetime (over 2000 h) in their group. The electrochemical performance of Na@nPU is presented in Figure S10, and Na@50PU shows the best electrochemical performances, demonstrating an overpotential of ≈ 40 mV (vs Na^+/Na) for over 800 h.

As the next step, each of the optimized thicknesses in each sample group is selected for further electrochemical performance tests and comparisons, as shown in Figure 2. Bare Na metal foil symmetrical cells are assembled as well as the reference samples. Figure 2(a) shows the electrochemical performance of symmetrical cells of Na@10Zn,PU, Na@25Al,PU, Na@50PU, and bare Na, under the current density of 3 mA cm^{-2} and with the capacity of 1mAh cm^{-2}. These results show that the initial Na stripping/plating overpotential of the bare Na foil sample is approximately 20 mV (vs Na^+ /Na) and rapidly increases to over 300 mV (vs Na^+/Na) after ~ 65 h indicating that the bare Na foil is unstable. In comparison, while the initial over-potentials of the remaining samples are very similar to that of the bare Na, their lifetimes are significantly longer, indicating that the stability of the Na metal interface is enhanced due to the presence of Al or Zn doped PU or pure PU layers. The remarkable stability of the Na@10Zn,PU sample is noteworthy, which exhibits a low overpotential of approximately 20 mV (vs Na^+/Na) even after approximately 3100 hours of continuous operation without any instances of short circuits, demonstrating the longest-lasting stability among the three coated samples.

Furthermore, when the current density is increased to 5 mA cm^{-2} (as shown in Figure 2(b)), the bare Na sample experiences an even quicker short circuit within approximately 40 hours of electrochemical cycling. Compared to bare Na, the other three samples present a prolonged cycling performance, even if Na@50PU has a fluctuating voltage profile during the Na stripping/plating process with soft short-circuiting of the cell occurring after 450 h. For Na@10Zn,PU and Na@25Al,PU, they have a better electrochemical performance with a similar low initial overpotential of about 30 mV (vs Na^+/Na) and stable overpotential during cycling, indicating single metal dopant in polyurea could enhance the chemical/electrochemical stability of artificial SEI. Differing from Na@25Al,PU, Na@10Zn,PU shows extremely stable electrochemical cycling performance without any obvious overpotential change from the initial stage, even over 900 h. Furthermore, the symmetrical cells are conducted in extremely high current density (10 mA cm^{-2}) with the capacity of 1 mAh cm^{-2} (as shown in Figure 2(c)). Interestingly, Na@10Zn,PU still shows

This article is protected by copyright. All rights reserved.

Author Manuscript

the best electrochemical performance with a stable overpotential of about 50 mV over 100 h with negligible change. Furthermore, it is observed that a minor fluctuation in the voltage profiles during the initial cycle is apparent because of the remarkably high current density. This phenomenon can be attributed to the formation of the initial SEI film, which occurs due to the reaction between the surface of the Na anode and the electrolyte. The electrochemical performance of all four group samples remains consistent with previous conditions, indicating the advantages provided by the presence of metal dopants in the polyurea and better chemical/electrochemical stability of the Zn-doped polyurea layer on Na metal foils. From the local magnification images (Figure S11, S12 and S13) obtained at three different current densities, it is evident that the overpotential of Na@10Zn,PU remains consistently stable at a certain value throughout the discharge or charge process, whereas Na@25Al,PU or Na@50PU shows clear fluctuation peaks of overpotential during charge and discharge cycles. The electrochemical performances (symmetrical cells) of reported literature on the design of artificial coatings for Na metal anode are summarized in Figure 2e. Compared to the previous studies, our design of Zn-doped PU coating layer as the artificial interface for Na metal anode demonstrates outstanding stability at high current density, even up to 10 mA cm^{-2}.

Electrochemical impedance spectroscopy (EIS) was conducted to assess the interfacial resistance of Na metal anodes, and EIS results are presented in Figure S14. In the Nyquist plots, the relationship between interfacial resistance and frequency was presented. It is observed that the interfacial resistance of bare Na is lower compared to Na samples with metal dopant PU coating, as shown in Figure S14(a). Specifically, the Na@10Zn,PU sample exhibited significantly higher interfacial resistance due to the non-ionic conductive nature of the PU layer. However, after 30 electrochemical cycles at a current density of 10 mA cm^{-2} with a capacity of 1 mAh cm^{-2}, the interfacial resistance of the Na samples with coating layers decreased significantly compared to the bare Na sample. This suggests that the coating layers underwent a sodiation process during the initial cycles, as illustrated in Figure S14(b) (which shows an enlarged view of Figure S11(c)). Notably, among the three coated samples, Na@10Zn,PU exhibited the lowest interfacial resistance, aligning with expectations and previous electrochemical results, which indicates that the Zn dopant within the PU structure is more favorable for Na^+ deposition than the Al dopant.

The nucleation and deposition behavior of Na has a significant effect on cycling reversibility. To further investigate and evaluate the cycling stability and reversibility of the Na metal anode, Coulombic efficiency (CE) and nucleation overpotentials of Na deposition

This article is protected by copyright. All rights reserved.

Author Manuscript

tests are conducted. To assess CEs, we utilized Cu foil as the working electrode in two different forms: with and without coating. The Cu foils with coating are individually denoted as Cu@10Zn,PU, Cu@25Al,PU, Cu@50PU. In these evaluations, Na foils are employed as the counter electrodes. The electrolyte used in symmetrical cells is still used in CE tests. Figure 2d shows the results of the CE test at a current density of 0.5 mA cm^{-2} with a capacity of 0.5 mAh cm^{-2}. For bare Cu, the initial CE performance is unstable, and its CE value fluctuates between 100 %. After that, CE drops below 100 % and becomes scattered only after 20 cycles, whereas Cu@50PU retained a high CE of ≈99.8% without an obvious decrease in the first 20 cycles. For Cu@10Zn,PU, it shows the best CE performance which can sustain a high CE of about 99% and keep extremely stable over 70 cycles without any obvious fluctuation. In addition, the nucleation overpotentials of Na deposition after 5 plating/stripping cycles on the Cu foils whose nomination are the same as those samples in CE tests are evaluated at the current density of 0.5 mA cm^{-2} with a capacity limitation of 0.5 mAh cm^{-2}, and the results are shown in Figure S15. Typically, the sodiophilicity of the substrate promotes the uniform nucleation and deposition of Na, resulting in a reduced nucleation overpotential.[28] The nucleation overpotential for Na deposition on Cu@10Zn,PU is 13.9 mV, which is evidently lower than other nucleation overpotentials. When we compare the charging curve of Cu@10Zn,PU with that of bare Cu, it can be observed that the curve of Cu@10Zn,PU almost overlap, indicating that Na can be effectively and consistently plated and stripped on the Cu@10Zn,PU electrode for the duration of the 5 cycles. Figure S16 shows the corresponding overpotential of Na/Cu half cells of CE measurements with different coatings as well as bare Cu. Highly stable Na plating/stripping cycling for more than 200 hours with no internal short-circuiting corresponds to the results of approximately 99.4% average CE for more than 60 cycles using Cu@10Zn,PU. In contrast, significant fluctuations in overpotential were observed with bare Cu, corresponding to its low CE values.

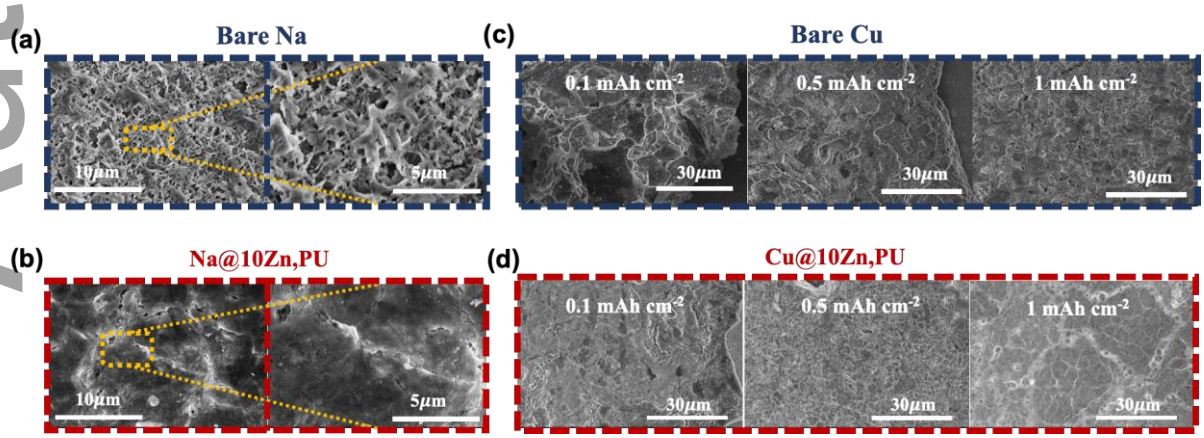
To investigate the feasibility of metal-doped PU Na anode for Na metal batteries, the electrochemical performance of full cells with Prussian blue analogs (PBAs) cathode was conducted. The PBAs-Na cells using bare Na and Na@10Zn,PU were cycled at 5 C to evaluate the influence of the coating on Na anodes (Figure 2f). In the initial stages, the bare Na exhibited a capacity comparable to that of Na@10Zn,PU. However, a pronounced and rapid capacity decay was observed after around 900 cycles for bare Na-PBAs full cell. The specific capacity of the bare Na-PBAs full cell only maintains less than 40 mAh g^{-1} after 2000 cycles. In contrast, the Na@10Zn,PU-PBAs cell demonstrated a remarkable capacity

This article is protected by copyright. All rights reserved.

Author Manuscript

retention of 65 mAh g^{-1} after 2000 cycles. The results of full cells are consistent with the trend observed in the previous electrochemical stability tests, demonstrating that the Na@10Zn,PU significantly contributes to improving the overall cell capacity retention.

To investigate the electrochemical stability of the interface in solid-state Na batteries, Na-Na symmetric cells utilizing Na_3SbS_4 (NAS) solid-state electrolyte (SSE), with and without an MLD coating, were tested at room temperature. NAS was selected because of high ionic conductivities and NAS was synthesized with the procedures following reported studies.[29] Powder X-ray diffraction patterns (XRD) of the synthesized NAS, as shown in Figure S18, exhibit diffraction peaks consistent with previously reported NAS (t-Na_3SbS_4: ICSD: PDF# 01-085-8198). Furthermore, the room-temperature ionic conductivity of NAS is measured as 1.7×10^{-3} S cm^{-1}, as shown in Figure S19. The cells were subjected to charging and discharging at a current density of 0.3 mA cm^{-2} and an areal capacity of 0.1 mAh cm^{-2}. In Figure S20, it is evident that the bare Na symmetric cell shows a significant increase in overpotential during the initial plating/stripping process, increasing from 0.44 V to 3.0 V, which can be attributed to undesirable side reactions occurring between Na metal and NAS. In contrast, it is observed that the initial charging/discharging overpotential of Na@10Zn,PU from the local magnification of the voltage profile (Figure S20) is approximately 0.2 V, whereas bare Na exhibits an initial overpotential of approximately 0.5 V. After 25 h cycling, the overpotential of Na@10Zn,PU stabilizes at around 0.8 V and this stable performance can maintain for up to 180 hours, which significantly lower than the approximately 2.5 V reached by bare Na. It indicates that the Zn-doped PU layer coating not only plays a significant role in the Na anode interface of liquid-state batteries but also exhibits remarkable electrochemical stability for the Na anode in solid-state batteries with NAS electrolyte systems.



This article is protected by copyright. All rights reserved.

Figure 3. Top-view SEM images of a) bare Na foil and b) Na@10Zn,PU after electrochemical cycling (30 cycles). Na nuclei deposited on c) bare Cu foil and d) Cu@10Zn,PU at a current density of 0.5 mA cm^{-2} with an areal capacity of 0.1, 0.5 and 1 mAh cm^{-2}, respectively.

In order to explore the impact of metal dopant PU coatings on improving cycling stability, the morphology of Na@10Zn,PU, Na@25Al,PU, Na@50PU and bare Na samples are analyzed using scanning electron microscopy (SEM) before and after completing 30 charge/discharge cycles at 5 mA cm^{-2} with the capacity of 1 mAh cm^{-2}, shown in Figure 3(a), (b), Figure S21, and Figure S22. In the top-view image of bare Na after cycling, Na dendrites are observed (Figure 3(a)) and the higher-magnification image reveals a porous structure, resulting from the significant volume expansion and contraction during the charge/discharge process. Additionally, irregular structures in the top-view images suggest the non-uniform plating and stripping of Na during the electrochemical process. These irregular Na structures tend to accumulate during subsequent plating and stripping processes, leading to increased polarization at the interface and ultimately accelerating cell failure. In comparison to the bare Na sample, the Na@10Zn,PU sample after cycling (Figure 3(b)) did not show prominent porous structures or dendrites on the electrode surface. The surface of Na@10Zn,PU appears considerably flatter than that of bare Na. Furthermore, from a higher-magnification image by contrast, the surface of Na@10Zn,PU appears remarkably smooth, with no observed formation of dendritic or mossy-like structures seen in the bare Na. Figure S21 shows the morphology of Na@10Zn,PU, Na@25Al,Pu and Na@50PU before-cycling. Even if some cracks on the surface of Na@10Zn,PU can be observed, the enlarged figure of the sample shows the surface is much denser and flatter than that of Na@25Al,PU and Na@50PU. More porous and mossy-like structures can also be observed on the surface of after-cycling Na@25Al,PU and Na@50PU, respectively, shown in Figure S22 compared to the Na@10Zn,PU after cycling. In contrast, the surface morphology of the coated samples is notably smoother, and more uniform compared to the bare Na sample. These results indicate that the Na metal anode with a single metal dopant PU coating, particularly the Zn dopant PU, forms a highly robust SEI during the electrochemical cycling process.

To study the morphology evolution of Na nuclei during electrodeposition, Cu electrodes were examined after depositing fixed amounts of sodium (0.1, 0.5, 1mAh cm^{-2}) galvanostatically at constant current densities of 0.5 mA cm^{-2}. Figures 3(c) and 3(d) show ex-

This article is protected by copyright. All rights reserved.

Author Manuscript

Author Manuscript

situ SEM images of the morphology of Na metal growths deposited on bare Cu and Cu@10Zn,PU in the ether-based electrolyte. At a low capacity of 0.1 mAh cm^{-2}, the Na growths are uniformly distributed on Cu foil without any obvious isolated particles and dendrites, which is different from the morphology of Li deposition on Cu foil [28]. By contrast, with the amount of Na deposition increasing, the morphology of the Na deposition on bare Cu electrode remains rough and exhibits cracks, creating spots for the growth and propagation of dendritic Na. After 1 mAh cm^{-2} of Na deposition, the Na deposition on bare Cu almost covers the whole Cu surface but there are still some voids remaining, and some areas are observed to stack in a vertical direction, forming a mossy-like morphology. Compared to that of bare Cu, the surface of Na deposition on Cu@10Zn,PU is flatter and smoother with no formation of dendritic or mossy Na, which is one of the key factors contributing to the significant improvement in electrochemical performance. The morphologies of Na deposition on Cu@25Al,PU and Cu@50PU foils are shown in Figures S23 and S24. From top-view SEM images, the morphology of Na deposition on Cu@25Al,PU is flatter than that of Cu@50PU but bumpier than that of Cu@10Zn,PU, and more distorted bulk Na and cracks are shown in the images of Cu@50PU. This morphological evolution trend corresponds to the results of electrochemical performance tests, which indicate that metal dopant PU SEI could facilitate uniform Na deposition. In addition, the distinctive ultra-uniform Na deposition for Zn-doped PU SEI could be attributed to the fact that Zn metal dopant provides sodiophilic sites in the polyurea SEI structure.

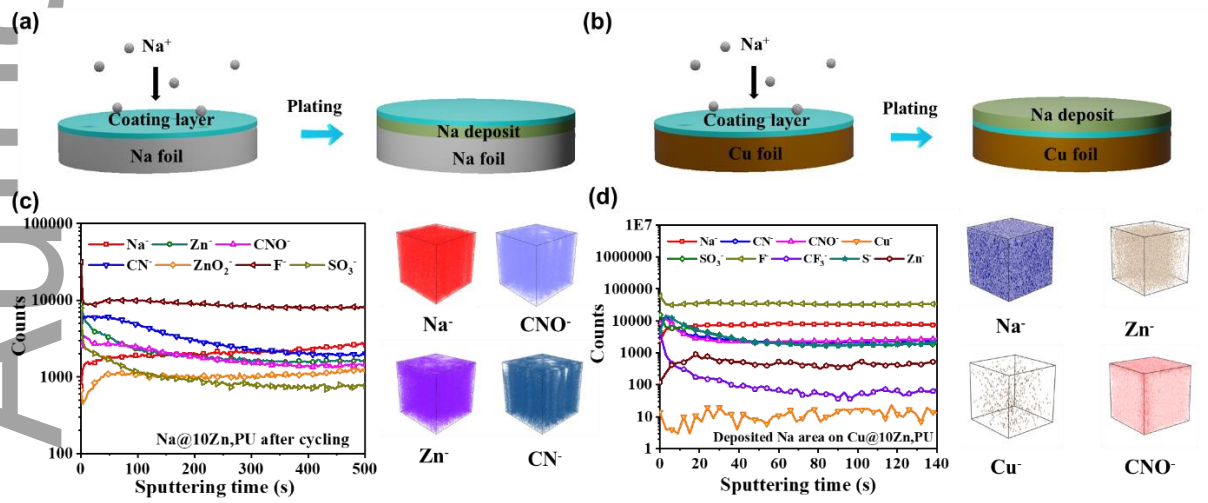


Figure 4. a,b) Schematic diagram of Na plating on different substrates. ToF-SIMS secondary ion depth profiles and corresponding 3D rendering images of c) Na@10Zn,PU

This article is protected by copyright. All rights reserved.

after electrochemical cycling (30 cycles), and d) deposited Na area on Cu@10Zn,PU at a current density of 0.5 mA cm^{-2} with an areal capacity of 0.5 mAh cm^{-2}.

To understand the interfacial compositional changes after cycling, RBS and ToF-SIMS measurements were carried out for various samples. Figure S25-S26 presents the RBS spectra and ToF-SIMS results of bare Na after cycling at a current density of 10 mA cm^{-2} with a capacity limit of 1 mAh cm^{-2}. It can be seen that a noticeable infiltration of F^- ions from the electrolyte of the bare Na sample, especially with prolonged sputtering time (over 500 s). Furthermore, the presence of strong signals from CF_3^- and SO_3^- secondary ion species is observed, indicating the decomposition of electrolyte components and the formation of a thick dead Na layer. The RBS results for Na@10Zn,PU after cycling indicate that Zn is still detected from the top surface to 100 nm depth, demonstrating that Zn-doped PU could facilitate Na diffusion into the PU layer during the cycling (Figure S27). More detailed information is obtained from ToF-SIMS results including secondary ion depth profiles and corresponding 3D rendering images for Na@10Zn,PU, Na@25Al,PU and Na@50Pu after cycling at a current density of 10 mA cm^{-2} with a capacity limit of 1 mAh cm^{-2}. From Figure 4(c) for Na@10Zn,PU, the species of Zn^-, CN^- and CNO^- present strong signals from the top surface and reach a near-steady level after 100 s Cs^+ sputtering, which has minimal variations compared to the Na@10Zn,PU before cycling. It is pertinent to note that the thickness of Na@10Zn,PU coating layers can be approximated as around 20 nm after cycling. This is clear evidence that the Na@10Zn,PU coating maintains a stable structure during the electrochemical process and reduces the side reactions between the electrolytes and Na metal anode. Since the feature species (Zn^-, CN^- and CNO^-) are observed from the top surface, the Na metal is expected to be deposited underneath the Na@10Zn,PU coating layer, indicating the Na@10Zn,PU coating layer is involved as an artificial SEI. Similar phenomena can be observed for Na@25Al,PU and Na@50Pu after cycling (Figure S28 and S29). Both Na@25Al,PU and Na@50Pu coatings are electrochemically stable after cycling with thicknesses of about 20 nm and 10 nm, respectively. When the PU-based interfaces are deposited on the Na metal anode, they act as artificial SEI, regulating the Na deposition and reducing the side reactions between the electrolytes and the Na metal anode.

Interestingly, when the PU-based coatings are deposited on the Cu current collector for half-cell study, the functions of the PU-based coatings are different compared to that of the coating on Na metal anodes. In the Na-Cu half cell, the surface of the Cu current collector

This article is protected by copyright. All rights reserved.

Author Manuscript

cannot be totally covered with deposited Na when the capacity is 1 mAh cm^{-2}. To have a deep understanding of the different roles, we conducted both SEM-EDS mapping and ToF-SIMS analysis for Cu@10Zn,PU and Cu@25Al,PU on the deposited Na area and uncovered Cu area, as shown in Figure 4(d) and S30-S34. From the SEM images in Figure S30, it can be observed that there are deposited Na areas and uncovered Cu areas when the deposition capacity is 1 mAh cm^{-2}. From the EDS results for Cu@10Zn,PU surface, the Zn signal map reveals that there is very little Zn distribution on deposited Na areas but a stronger signal from the uncovered Cu areas. Figure 4(d) and S31 illustrate the ToF-SIMS result from the deposited Na area and uncovered Cu areas for Cu@10Zn,PU, respectively. Clear differences can be observed from the Zn^- signal comparison, in which a trace Zn^- signal is detected on the deposited Na area of Cu foil but strong Zn^- species are seen from the uncovered Cu surface. It indicates that the Zn-PU layers are not on top of the deposited Na, instead, the Zn-PU layers play a role in modifying the Cu current collector and regulating the Na deposition behaviour, which is consistent with the discussion above for Na nucleation on Cu foil [30]. Similar results were obtained for Cu@25Al,Pu. However, the situation is different for Zn/Al-PU coating layers on Na metal from on Cu foil. A comparison of the ToF-SIMS depth profile for Na@10Zn,PU after cycling (Figure 4(c)) shows that the Zn^- signal intensity is much stronger than that of the Na-deposited regions of Cu@10Zn,PU which showing trace intensity (Figure 4(d)). As indicated in Figure 4(a, b), when the Zn-PU layer is coated on the Na metal anode, the Zn-PU coating involves into the formation of artificial SEI for reducing the side reactions between the Na metal with electrolyte, regulating Na deposition and preventing the Na dendrite formation, in which Na is deposited underneath the Zn-PU coating. In contrast, when the Zn-PU layer is deposited on the Cu current collector, the Na is deposited on top of Zn-PU layer with the dendrite-free structure. Similar results of SEM-EDS mapping and ToF-SIMS analysis for Na@25Al,Pu and Cu@25Al,PU are shown in Figure S28 and S32-S34. The presence of Al^- is nearly imperceptible on the deposited Na area of Cu@25Al,PU (Figure S33), however, the variation trend of Al^- signal counts is clearly shown in the depth profile on the Na@25Al,PU (Figure S28). Similar phenomena and results are reported in the literature when using the nanoscale coatings (such as ALD/MLD-deposited layers) for different substrate of Cu foils and alkaline metals [31].

Author Manuscript

This article is protected by copyright. All rights reserved.

Author Manuscript

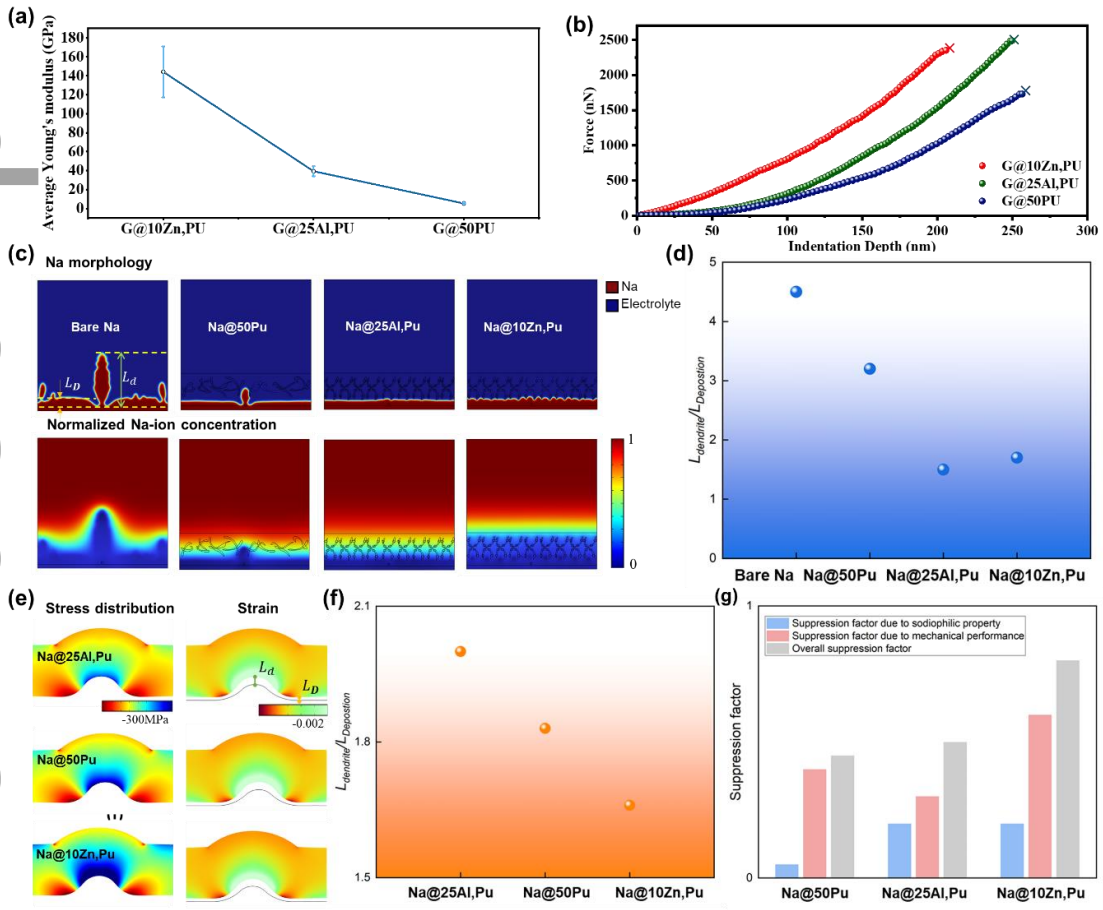


Figure 5. Phase-field simulation results of the impact of ionic transportation capability and mechanic property. a) The morphology of deposited Na and normalized Na-ion concentration using bare Na foil and Na@10Zn,PU, Na@25Al,PU, and Na@50PU. b) The relative dendrite penetration length (the ratio of Na dendrite length and average deposition thickness) of three hybrid protective layers of different ionic conductive. c) Stress distribution and strain on three hybrid protective layers. d) The relative dendrite penetration length under the electrochemical-mechanic model by inputting Young's modulus data measured experimentally. e) Overall suppression factor of dendrite growth by three hybrid protective layers, including the effect of sodiophilic property and mechanical property. f) Young's moduli of metal-doped and pure PU films measured from AFM deflection test. g) Force–deflection (F–δ) curves from the AFM deflection test to capture the fracture forces of the nanofilms (marked crosses indicate the points of failure). Presented F–δ curves are selected as representatives from ten individual measurements in each case on different freestanding films.

This article is protected by copyright. All rights reserved.

Author Manuscript

The mechanical properties of MLD metal-doped PU films were investigated by conducting atomic force microscopy (AFM) deflection tests (more details of the AFM measurement and analysis can be found in the corresponding Figure S35). To understand the influence of Zn-crosslinker on PU films toward their mechanical properties, three groups of samples were prepared: 10 cycles of Zn-doped PU (G@10Zn,PU), Al-doped PU (G@25Al,PU) and pure PU (G@50PU). Each nanofilm was individually deposited onto suspended monolayer graphene covering a perforated Si_3N_4-based transmission electron microscopy (TEM) grid (Figure S35). Both elastic and fracture AFM deflection tests were performed on the three groups of nanofilms. Young's modulus was extracted by fitting the force-displacement curve from AFM elastic deflection tests to an analytical solution of a suspended film over a circular hole developed by Lee et al [32]. The average Young's moduli for each case (over ten independent measurements performed for each sample group) are plotted in Figure 5(a). It is clear that G@10Zn,PU exhibits the highest stiffness (~117.3-171.1 GPa) followed by G@25Al,PU (~34.1-44.6 GPa), and G@50PU (~4.7-5.9 GPa) is the least stiff among the three sample groups. Further, fracture AFM deflection tests were performed to capture the failure forces needed to cause the ultimate fracture of the nanofilms. Representative force-displacement curves of each nanofilm case during the fracture deflection tests are shown in Figure 5(b). A similar trend is observed in terms of their fracture forces where G@10Zn, PU and G@25Al, PU exhibit fracture forces ~2500 nN, while G@50PU fails at a much lower force of ~1500nN. These results suggest that single metal crosslinkers (both Zn and Al) can enhance the stiffness of the polyurea structure compared to pure polymer. The superior mechanical performance of MLD metal-doped PU films effectively inhibits dendrite growth on the Na-metal anode interface, aligning with the results from the measurements of electrochemical performance.

To investigate the impact of metal-doped film's ionic transportation capability (i.e., ion diffusion coefficient) and mechanic property (i.e., Young's modulus) on Na deposition, the electrochemical-mechanic phase field model is carried out. Figure 5(c) shows the morphology of deposited Na and the distribution of the normalized Na-ion with different films. Herein, an initial Na perturbation is introduced to the system. The structure of the different coating layers originates from Figure 1(a), where a highly ordered architecture is presented in hybrid metal-doped films compared to that of pure polyurea films [43]. And the ratio of the Na-ion diffusion coefficient in Na@10Zn,PU, Na@25Al,PU, Na@50PU, and electrolyte is 600:100:1:4 [44]. A much more homogeneous Na deposition in Na@25Al,PU

This article is protected by copyright. All rights reserved.

and Na@10PZn,PU is observed. This is attributed to the fact that the sodiophilicity in the hybrid film (induced by metal ions) promotes the Na ion diffusion, resulting in a smoother Na distribution at the interface. Herein, the relative dendrite penetration length (i.e. the ratio of Na dendrite length and average deposition thickness) is introduced to quantify the effect of dendrite suppression with different films, as illustrated in Figure 5(c). As the ion diffusion coefficient is raised to a certain range, the ability of the dendrite suppression contributed by the diffusion coefficient reaches the limit (Figure 5(d)). This leads to the relative dendrite penetration length becoming stable, i.e., a relatively homogeneous Na deposition. The Young's modulus of the three coating layers is derived from the experimentally measured data: Na@10Zn,PU (144.1 GPa) > Na@50PU (100.8 GPa) > Na@25Al,PU (78.6 GPa). As depicted in Figure 5(e) and Figure S38, the compressive stress at the tip of the perturbation increases with higher Young's modulus. The high compressive stress inhibits dendrites by slowing down the deposition rate. Also, the relative dendrite penetration length declines with the increase of Young's modulus (Figure 5(f)). Figure 5(g) compares the overall suppression factor of three films on dendrite growth, including the effect of sodiophilic property and mechanical property. Na@50PU has a comparable dendrite suppression factor on Na@25Al,PU, although its ion diffusion coefficient is much lower than that of Na@25Al,PU, which is consistent with the electrochemical performance demonstrated in Figure 2. This is attributed to the fact that Young's modulus of Na@50PU is 1.28 times higher than that of the Na@25Al,PU. Consequently, mechanical property plays a more important role in suppressing the dendrite. As expected, Na@10Zn,PU shows the most favorable performance in inhibiting dendrites, considering its excellent mechanical stability that can generate sufficiently high compressive stress and great sodiophilic properties that enable faster ion diffusion and more homogeneous deposition.

Conclusion

In this study, we have successfully demonstrated the effectiveness of nanoscale polymer coatings in fabricating a stable artificial SEI for high-performance Na metal anodes. By precisely controlling the film composition through MLD, we have developed metal-doped polyurea coatings with enhanced stiffness and improved sodiophilic sites. These coatings have enabled the operation of Na metal anodes at ultra-high current density (10 mA cm^{-2}) with negligible increase in overpotential. Notably, the artificial SEI has effectively suppressed dendrite growth and minimized the accumulation of "dead Na". It is also

This article is protected by copyright. All rights reserved.

Author Manuscript

interesting to demonstrate that the roles and functions of the coating on the Na metal anode and Cu current collector are different. Additionally, we have experimentally investigated the influence of different interface mechanical stabilities on electrochemical performance. Our findings not only demonstrate the successful development of a stable artificial SEI for Na metal anodes but also highlight the potential of our approach in providing sodiophilic sites and mechanically stable interfaces for the design and fabrication of next-generation high-performance energy storage systems. This work opens up new avenues for advancing Na metal anode battery technologies and brings us closer to realizing their full potential in practical applications.

Contributions

Y.Z. and E.J. conceived and designed the experiments. E.J. prepared samples and carried out the main experiments. K.T., H.Y., and L.C. carried out the Phase-field simulations. H.H and C.C conducted the AFM measurements. G.P. and L.G helped with RBS testing and simulation. Y.W., P.P., S.K., and F.D. involved in the data analysis. E.J. wrote and Y.Z. revised the paper. All the authors commented on the manuscript.

Acknowledgments

Y. Zhao acknowledges support from the Natural Science and Engineering Research Council of Canada (NSERC), the Canada Foundation for Innovation (CFI), the University of Western Ontario (UWO) and Carbon Solutions, a Strategic Priorities Fund project of the University of Western Ontario (UWO). L. Goncharova acknowledges support from the Natural Science and Engineering Research Council of Canada (NSERC) (RGPIN-2020-06679).

Reference

[1] K. Chayambuka, G. Mulder, D. L. Danilov, P. H. L. Notten, *Advanced Energy Materials* **2020**, 10.

[2] a)A. Rudola, R. Sayers, C. J. Wright, J. Barker, *Nature Energy* **2023**, 8, 215; b)Y. Fang, L. Xiao, Z. Chen, X. Ai, Y. Cao, H. Yang, *Electrochemical Energy Reviews* **2018**, 1, 294; c)J.-M. Tarascon, *Joule* **2020**, 4, 1616.

[3] H. Ye, Y. Li, *InfoMat* **2022**, 4.

[4] a)W. Yao, P. Zou, M. Wang, H. Zhan, F. Kang, C. Yang, *Electrochemical Energy Reviews* **2021**, 4, 601; b)L. Fan, X. Li, *Nano energy* **2018**, 53, 630; c)P. Chen, C. Y. Wang, T. Y. Wang, *Materials Research Letters* **2022**, 10, 691.

This article is protected by copyright. All rights reserved.

Author Manuscript

[5] a)C. Bao, B. Wang, P. Liu, H. Wu, Y. Zhou, D. Wang, H. Liu, S. Dou, *Advanced Functional Materials* **2020**, 30; b)T. Wang, Y. Hua, Z. Xu, J. S. Yu, *Small* **2022**, 18, e2102250.
[6] B. Lee, E. Paek, D. Mitlin, S. W. Lee, *Chem Rev* **2019**, 119, 5416.
[7] a)C. Zhao, Y. Lu, J. Yue, D. Pan, Y. Qi, Y.-S. Hu, L. Chen, *Journal of Energy Chemistry* **2018**, 27, 1584; b)Y. Zhao, K. R. Adair, X. Sun, *Energy & Environmental Science* **2018**, 11, 2673.
[8] W. Liu, P. Liu, D. Mitlin, *Advanced Energy Materials* **2020**, 10, 2002297.
[9] a)W. Luo, C. F. Lin, O. Zhao, M. Noked, Y. Zhang, G. W. Rubloff, L. Hu, *Advanced Energy Materials* **2016**, 7; b)Y. Zhao, L. V. Goncharova, A. Lushington, Q. Sun, H. Yadegari, B. Wang, W. Xiao, R. Li, X. Sun, *Adv Mater* **2017**, 29; c)Y. Zhao, L. V. Goncharova, Q. Zhang, P. Kaghazchi, Q. Sun, A. Lushington, B. Wang, R. Li, X. Sun, *Nano Lett* **2017**, 17, 5653; d)D. Lei, Y. B. He, H. Huang, Y. Yuan, G. Zhong, Q. Zhao, X. Hao, D. Zhang, C. Lai, S. Zhang, J. Ma, Y. Wei, Q. Yu, W. Lv, Y. Yu, B. Li, Q. H. Yang, Y. Yang, J. Lu, F. Kang, *Nat Commun* **2019**, 10, 4244; e)Z. Xu, J. Yang, T. Zhang, L. Sun, Y. Nuli, J. Wang, S. i. Hirano, *Advanced Functional Materials* **2019**; f)Y. Zhao, J. Liang, Q. Sun, Lyudmila V. Goncharova, J. Wang, C. Wang, K. R. Adair, X. Li, F. Zhao, Y. Sun, R. Li, X. Sun, *Journal of Materials Chemistry A* **2019**, 7, 4119; g)Y. Shuai, J. Lou, X. Pei, C. Su, X. Ye, L. Zhang, Y. Wang, Z. Xu, P. Gao, S. He, Z. Wang, K. Chen, *ACS Applied Materials & Interfaces* **2022**, 14, 45382; h)S. Wei, S. Choudhury, J. Xu, P. Nath, Z. Tu, L. A. Archer, *Advanced Materials* **2017**, 29, 1605512.
[10] a)Q. Chen, Z. Hou, Z. Sun, Y. Pu, Y. Jiang, Y. Zhao, H. He, T. Zhang, L. Huang, *ACS Applied Energy Materials* **2020**, 3, 2900; b)S. Wang, Y. Jie, Z. Sun, W. Cai, Y. Chen, F. Huang, Y. Liu, X. Li, R. Du, R. Cao, G. Zhang, S. Jiao, *ACS Applied Energy Materials* **2020**, 3, 8688.
[11] K. N. Wood, M. Noked, N. P. Dasgupta, *ACS Energy Letters* **2017**, 2, 664.
[12] a)X. Shen, R. Zhang, X. Chen, X. B. Cheng, X. Li, Q. Zhang, *Advanced Energy Materials* **2020**, 10; b)T. Krauskopf, F. H. Richter, W. G. Zeier, J. Janek, *Chem Rev* **2020**, 120, 7745; c)B. Lee, E. Paek, D. Mitlin, S. W. Lee, *Chemical Reviews* **2019**, 119, 5416; d)J. Kim, J. Kim, J. Jeong, J. Park, C.-Y. Park, S. Park, S. G. Lim, K. T. Lee, N.-S. Choi, H. R. Byon, C. Jo, J. Lee, *Energy &Environmental Science* **2022**, 15, 4109.
[13] a)W. Cao, J. Lu, K. Zhou, G. Sun, J. Zheng, Z. Geng, H. Li, *Nano Energy* **2022**, 95; b)L. Fan, B. Sun, K. Yan, P. Xiong, X. Guo, Z. Guo, N. Zhang, Y. Feng, K. Sun, G. Wang, *Advanced Energy Materials* **2021**, 11; c)Y. Gao, Z. Yan, J. L. Gray, X. He, D. Wang, T. Chen, Q. Huang, Y. C. Li, H. Wang, S. H. Kim, T. E. Mallouk, D. Wang, *Nat Mater* **2019**, 18, 384; d)S. Li, L. Fan, Y. Lu, *Energy Storage Materials* **2019**, 18, 205; e)F. Wu, Z. Wen, Z. Zhao, J. Bi, Y. Shang, Y. Liang, L. Li, N. Chen, Y. Li, R. Chen, *Energy Storage Materials* **2021**, 38, 447.
[14] Y. Sun, M. Amirmaleki, Y. Zhao, C. Zhao, J. Liang, C. Wang, K. R. Adair, J. Li, T. Cui, G. Wang, R. Li, T. Filleter, M. Cai, T. K. Sham, X. Sun, *Advanced Energy Materials* **2020**, 10, 2001139.
[15] S. Li, M. Jiang, Y. Xie, H. Xu, J. Jia, J. Li, *Adv Mater* **2018**, 30, e1706375.
[16] Y. Liu, D. Lin, P. Y. Yuen, K. Liu, J. Xie, R. H. Dauskardt, Y. Cui, *Adv Mater* **2017**, 29.
[17] a)P. Pirayesh, K. Tantratian, M. Amirmaleki, F. Yang, E. Jin, Y. Wang, L. V. Goncharova, J. Guo, T. Filleter, L. Chen, Y. Zhao, *Adv Mater* **2023**, e2301414; b)Y. Zhao, M. Amirmaleki, Q. Sun, C. Zhao, A. Codirenzi, L. V. Goncharova, C. Wang, K. Adair, X. Li, X. Yang, F. Zhao, R. Li, T. Filleter, M. Cai, X. Sun, *Matter* **2019**, 1, 1215.

Author Manuscript

This article is protected by copyright. All rights reserved.

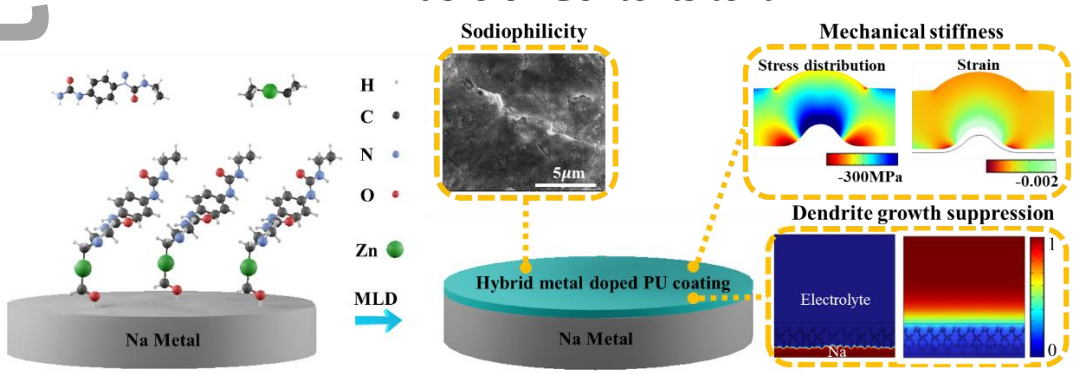
[18] a)B. Sun, P. Li, J. Zhang, D. Wang, P. Munroe, C. Wang, P. H. L. Notten, G. Wang, *Adv Mater* **2018**, e1801334; b)Y. Zhao, X. Yang, L. Y. Kuo, P. Kaghazchi, Q. Sun, J. Liang, B. Wang, A. Lushington, R. Li, H. Zhang, X. Sun, *Small* **2018**, 14, e1703717.
[19] a)Q. Chen, B. Liu, L. Zhang, Q. Xie, Y. Zhang, J. Lin, B. Qu, L. Wang, B. Sa, D.-L. Peng, *Chemical Engineering Journal* **2021**, 404; b)J. Han, G. He, *Small* **2021**, 17, e2102126; c)Z. Wang, X. Zhang, S. Zhou, K. Edström, M. Strømme, L. Nyholm, *Advanced Functional Materials* **2018**, 28; d)J. Wu, P. Zou, M. Ihsan-Ul-Haq, N. Mubarak, A. Susca, B. Li, F. Ciucci, J. K. Kim, *Small* **2020**, 16, e2003815; e)W. Yang, W. Yang, L. Dong, G. Shao, G. Wang, X. Peng, *Nano Energy* **2021**, 80.
[20] a)S. Tang, Y. Y. Zhang, X. G. Zhang, J. T. Li, X. Y. Wang, J. W. Yan, D. Y. Wu, M. S. Zheng, Q. F. Dong, B. W. Mao, *Advanced Materials* **2019**, 31, 1807495; b)S. Tang, Z. Qiu, X.-Y. Wang, Y. Gu, X.-G. Zhang, W.-W. Wang, J.-W. Yan, M.-S. Zheng, Q.-F. Dong, B.-W. Mao, *Nano Energy* **2018**, 48, 101; c)X. Chen, X. Zhou, Z. Yang, Z. Hao, J. Chen, W. Kuang, X. Shi, X. Wu, L. Li, S. Chou, *Chemical Science* **2024**.
[21] W. Liu, Z. Chen, Z. Zhang, P. Jiang, Y. Chen, E. Paek, Y. Wang, D. Mitlin, *Energy & Environmental Science* **2021**, 14, 382.
[22] Y. Sun, Y. Zhao, J. Wang, J. Liang, C. Wang, Q. Sun, X. Lin, K. R. Adair, J. Luo, D. Wang, R. Li, M. Cai, T.-K. Sham, X. Sun, *Advanced Materials* **2019**, 31, 1806541.
[23] Z. Wang, B. Liu, E. W. Zhao, K. Jin, Y. Du, J. J. Neeway, J. V. Ryan, D. Hu, K. H. L. Zhang, M. Hong, S. Le Guernic, S. Thevuthasan, F. Wang, Z. Zhu, *Journal of the American Society for Mass Spectrometry* **2015**, 26, 1283.
[24] Y. Sun, C. Zhao, K. R. Adair, Y. Zhao, L. V. Goncharova, J. Liang, C. Wang, J. Li, R. Li, M. Cai, T.-K. Sham, X. Sun, *Energy & Environmental Science* **2021**, 14, 4085.
[25] a)K. Che, P. Lyu, F. Wan, M. Ma, *Materials* **2019**, 12, 3636; b)H. Shinohara, F. Kitagawa, J. Mizuno, S. Shoji, O. Ohara, Y. Takahashi, A. Nakahara, K. Otsuka, *IET Nanobiotechnology* **2011**, 5, 136.
[26] a)S. M. N. Uddin, Y. Nagao, *Langmuir* **2017**, 33, 12777; b)Y. Sun, Y. Zhao, J. Wang, J. Liang, C. Wang, Q. Sun, X. Lin, K. R. Adair, J. Luo, D. Wang, R. Li, M. Cai, T. K. Sham, X. Sun, *Advanced Materials* **2019**, 31, 1806541.
[27] H. W. Nesbitt, G. M. Bancroft, G. S. Henderson, R. Ho, K. N. Dalby, Y. Huang, Z. Yan, *Journal of Non-Crystalline Solids* **2011**, 357, 170.
[28] A. Pei, G. Zheng, F. Shi, Y. Li, Y. Cui, *Nano letters* **2017**, 17, 1132.
[29] a)A. Banerjee, K. H. Park, J. W. Heo, Y. J. Nam, C. K. Moon, S. M. Oh, S. T. Hong, Y. S. Jung, *Angewandte Chemie* **2016**, 128, 9786; b)H. Wang, Y. Chen, Z. D. Hood, G. Sahu, A. S. Pandian, J. K. Keum, K. An, C. Liang, *Angewandte Chemie International Edition* **2016**, 55, 8551; c)L. Zhang, D. Zhang, K. Yang, X. Yan, L. Wang, J. Mi, B. Xu, Y. Li, *Advanced Science* **2016**, 3, 1600089.
[30] a)Z. Tu, M. J. Zachman, S. Choudhury, K. A. Khan, Q. Zhao, L. F. Kourkoutis, L. A. Archer, *Chemistry of Materials* **2018**, 30, 5655; b)S. T. Oyakhire, W. Huang, H. Wang, D. T. Boyle, J. R. Schneider, C. De Paula, Y. Wu, Y. Cui, S. F. Bent, *Advanced Energy Materials* **2020**, 10, 2002736; c)Y. Wang, H. Dong, N. Katyal, B. S. Vishnugopi, M. K. Singh, H. Hao, Y. Liu, P. Liu, P. P. Mukherjee, G. Henkelman, J. Watt, D. Mitlin, *Advanced Energy Materials* **2023**, 13.
[31] a)L. Chen, J. G. Connell, A. Nie, Z. Huang, K. R. Zavadil, K. C. Klavetter, Y. Yuan, S. Sharifi-Asl, R. Shahbazian-Yassar, J. A. Libera, A. U. Mane, J. W. Elam, *Journal of Materials Chemistry A* **2017**, 5, 12297; b)W. Luo, C. F. Lin, O. Zhao, M. Noked, Y. Zhang, G. W. Rubloff, L. Hu, *Advanced Energy Materials* **2017**, 7, 1601526.
[32] G.-H. Lee, R. C. Cooper, S. J. An, S. Lee, A. Van Der Zande, N. Petrone, A. G. Hammerberg, C. Lee, B. Crawford, W. Oliver, J. W. Kysar, J. Hone, *Science* **2013**, 340, 1073.

This article is protected by copyright. All rights reserved.

Author Manuscript

Author Manuscript

Table of Contents text



A metal-doped nanoscale polymeric film with improved sodiophilic sites and enhanced stiffness is developed by using the molecular layer deposition (MLD) technique. Metal crosslinkers in polymer chains ensure exceptional electrochemical/chemical stability for Na metal anodes, significantly extending lifespan at high current densities. The artificial SEI has effectively suppressed dendrite growth and minimized the accumulation of “dead Na”.

This article is protected by copyright. All rights reserved.